Available online at www.sciencedirect.com

ScienceDirect

Ceramics International 40 (2014) 14701–14712

CERAMICS INTERNATIONAL

www.elsevier.com/locate/ceramint

New insights into the properties of $K_xNa_{(1-x)}NbO_3$ ceramics obtained by hydrothermal synthesis

Leandro A. Ramajo[a], Fernando Rubio-Marcos[b], Adolfo Del Campo[b], Jose F. Fernández[b], Miriam S. Castro[a], Rodrigo Parra[a]

[a]Instituto de Investigaciones en Ciencia y Tecnología de Materiales (INTEMA), CONICET – UNMdP, J. B. Justo 4302, B7608FDQ Mar del Plata, Argentina
[b]Electroceramic Department, Instituto de Cerámica y Vidrio, CSIC, Kelsen 5, 28049 Madrid, Spain

Received 29 April 2014; received in revised form 10 June 2014; accepted 11 June 2014
Available online 18 June 2014

Abstract

Different reaction conditions for the hydrothermal synthesis of $K_xNa_{(1-x)}NbO_3$ (KNN) were studied. Samples were synthesized at 190 °C in a Teflon lined autoclave and the effects of different KOH/(KOH + NaOH) ratios (0–0.8) and total hydroxide concentration (2–8 N) on the microstructural and electrical properties of KNN were analyzed. A sodium rich phase with a monoclinic structure has been obtained, in which the orthorhombic phase coexists as detected by X-ray diffraction. These analyses also revealed that the x value in the $K_xNa_{(1-x)}NbO_3$ system gradually increases with the increasing KOH/(KOH + NaOH) ratio and total hydroxide concentration. Samples with higher potassium content showed higher density and improved electrical behavior. An exhaustive characterization by Confocal Raman Microscope allowed the observation of the ferroelectric domain structure in KNN ceramics. It was established that the grain boundaries constrain the 90° domain walls in order to reduce the stress accumulated by the orthorhombic and the monoclinic phase coexistence within the KNN grains.

Keywords: Hydrothermal synthesis; Lead-free piezoelectrics; Raman spectroscopy; Sodium potasium niobate

1. Introduction

The use of lead-free piezoelectric materials have gained much attention in recent years. Sodium potassium niobate $K_xNa_{1-x}NbO_3$ (KNN), a possible candidate for replacing $Pb(Zr_xTi_{1-x})O_3$ (PZT) in piezoelectric devices as a lead-free material, is appealing for piezoelectric applications because of its relatively low dielectric permittivity and high electromechanical coupling coefficient [1,2].

KNN is a combination of ferroelectric $KNbO_3$ and antiferroelectric $NaNbO_3$, and it forms a morphotropic phase boundary (MPB) for K contents of about 50% [3,4]. Although KNN is a promising piezoelectric material, there are some aspects that still call for attention: high densities (> 90% theoretical density) are difficult to attain during normal sintering and, K_2O and Na_2O easily evaporate at high temperatures [5–9].

Densification problems can be avoided by synthesizing nanosized powders with improved sintering activity prepared by sol–gel or hydrothermal processes [6,10,11]. Hydrothermal synthesis is considered as a good method for low-cost production of highly reproducible ceramic powders at moderate temperatures, which yields fine crystalline particles without any need for calcination or grinding unlike many high-temperature techniques [12]. The key factors governing the chemical reactions in hydrothermal processes have been recently discussed in a review article [13]. Concerning the hydrothermal synthesis of $(K,Na)NbO_3$, the effects of temperature, time, pH, precursors and KOH/NaOH ratio have been intensively studied during the last years [14–16]. However, there are a number of aspects that remain controversial with respect to the role of synthesized powders by the hydrothermal method on sinterability of the ceramics, and therefore, with the development of good ferroelectric properties in this system. Main difficulties are encountered in the synthesis of single-phase MPB composition. These phenomena are due to the fact that Na^+ cations react faster than K^+ cations with Nb^{5+} to

http://dx.doi.org/10.1016/j.ceramint.2014.06.059
0272-8842/

form $NaNbO_3$ perovskite. The production of pure $KNbO_3$–$NaNbO_3$ solid solution powder with an accurate composition of $K_{0.5}Na_{0.5}NbO_3$ by the hydrothermal method has been the focus of various studies [17,18].

The developments in the synthesis of ferroelectrics will not be complete without a proper choice of characterization tools for the study of ferroelectric features at the micro-nanoscale. Some of these techniques will be discussed in this work focusing on the combination of high spatial resolution scanning probe microscopy with chemical information based techniques, especially Confocal Raman Microscopy (CRM), as these are the novel characterization tools for the assessment of the ferroelectric and piezoelectric functionality at the micro-nanoscale. Raman spectroscopy is a useful technique for the characterization of KNN, not only for the detection of the crystalline phases present in a sample, but it is also highly sensitive to phase transitions. For instance, phase transitions that take place in the 10–300 K temperature range have been observed in $K_{0.2}Na_{0.8}NbO_3$ [19]. Furthermore, a recent paper has shown Raman spectra across the full set of four phases (cubic-tetragonal-orthorombic-rhombohedral) for a $(K_{0.5+\delta}Na_{0.5-\delta})NbO_3$ crystal with $\delta \sim 0.05$ [20]. Displacive phase transitions induced by the small crystallite size have also been evidenced by micro-Raman spectroscopy as variety of vibrational modes in $K_{0.5}Na_{0.5}NbO_3$ [21]. However, the ferroelectric domains in KNN ceramics have seldom been characterized by means of this technique [22–25].

This work aims to the (hydrothermal) synthesis of lead free ferroelectrics based on $K_xNa_{(1-x)}NbO_3$. The influence of the KOH/(KOH+NaOH) ratio and total hydroxide concentration in the reaction medium was studied in order to evaluate the effects on morphology, size, sinterability and crystallization of KNN. Besides, the ferroelectric domain structure was assessed by means of Confocal Raman Microscopy.

2. Experimental procedure

Selected reagents were analysis-grade Nb_2O_5 (Aldrich 99.8%), NaOH and KOH (BioPack 99.8%). KOH and NaOH aqueous solutions were prepared in different KOH/(KOH+NaOH) ratios (0–0.8) with total OH^- concentrations between 4 and 8 N. Then, 100 ml of these solutions were poured into a Teflon lined stain-less steel reactor along with 1 g Nb_2O_5. The closed reactor was heated in a silicone oil bath for 3 h at 190 °C, with constant stirring. The crystalline phases present in the obtained powders were assessed by X-ray diffraction, using a Philips PW1050/25 diffractometer running with CuK_α radiation, and by Raman spectroscopy with a Renishaw inVia microscope by means of the 514 nm Ar-ion laser line (50 mW nominal power).

Powders were uniaxially pressed into disks of 5 mm in diameter and 0.6 mm thick, approximately, and sintered at 1125 °C for 2 h in a Carbolite RHF17 furnace (equipped with an Eurotherm 2404 controller) with heating and cooling rates of 5 °C/min. The microstructural characterization of sintered, polished and metalized samples was completed by Scanning Electron Microscopy (SEM) using a JEOL JSM-6460LV microscope. Grain boundaries were previously exposed by thermal etching at 1075 °C for 10 min. The apparent density was measured by the Archimedes method and crystalline phases were assessed by XRD and Raman spectroscopy.

For electrical measurements silver electrodes were painted on both parallel sides of the sintered samples. Dielectric spectroscopy measurements were carried out with frequency response analyzers Hioki 3522-50 and 3535 LCR in the 100 Hz to 10 MHz frequency range. Finally, the ferroelectric nature of the ceramics was characterized using a hysteresis meter (RT 6000 HVS, RADIANT Technologies).

Raman analyses were performed using a Confocal Raman Microscope (Witec alpha-300R). Ceramic samples were polished and thermally etched at 950 °C for 5 min. Raman spectra were obtained using a 532 nm excitation laser and a 100× objective lens (NA=0.95). The incident laser power was 40 mW. The optical diffraction resolution of the Confocal Microscope was limited to about ~200 nm laterally and ~500 nm vertically. Raman spectral resolution of the system was 0.02 cm^{-1}. The sample was mounted on a piece-driven scan platform having 4 nm lateral and 0.5 nm vertical positional accuracy. The microscope base was also equipped with an active vibration isolation system, active 0.7–1000 Hz. Collected spectra were analyzed using Witec Control Plus Software.

3. Results and discussion

3.1. Characterization of synthesized powders

From the XRD patterns shown in Fig. 1(A), it could be determined that the powder obtained not using KOH corresponds to orthorhombic $NaNbO_3$ in agreement with the JCPDS 74-2440 file. Patterns from samples 0.2–0.8 KOH/(KOH+NaOH) ratios, with 4 N total OH^- concentration, show that these systems are similar to $K_{0.02}Na_{0.98}NbO_3$ (JCPDS 74-2024) and $K_{0.1}Na_{0.9}NbO_3$ (JCPDS 74-2025) solid solution structures. According to these XRD patterns, samples obtained from 0.2 and 0.4 mixtures are in good agreement with $K_{0.02}Na_{0.98}NbO_3$; whereas $K_{0.1}Na_{0.9}NbO_3$ is present in samples obtained with higher (0.5 and 0.6) KOH/(KOH+NaOH) ratios. Concerning the system with the highest (0.8) KOH/(KOH+NaOH) ratio, the peaks associated with Nb_2O_5 (JCPDS 07-0061 and 05-0352) and $NaNbO_3$ can be indexed to monoclinic symmetry and space group P2/m (JCPDS 74-2440). It can be concluded that niobium oxide did not completely dissolve under reaction conditions of 4 N total hydroxide concentration and 0.8 KOH/(KOH+NaOH) ratio.

Fig. 1(B) shows a magnification of the 45.5–47.5° 2θ region of the patterns in Fig. 1(A), showing peaks associated with the (200) and (020) crystallographic planes of a $K_xNa_{1-x}NbO_3$ monoclinic structure, which is in agreement with the phase diagram reported by Zhang et al. [23]. The lattice parameters were refined for sample 0.6 KOH/(KOH+NaOH) by using the monoclinic point group C2/M. The calculated parameters revealed a limited evolution of the lattice parameters, $a=3.924$ Å, $b=3.889$ Å, $c=3.920$ Å, and $\beta=89.53°$ ($\beta \sim 90°$). For systems with 0.6 KOH/(KOH+NaOH) ratio it can be suggested that two phases

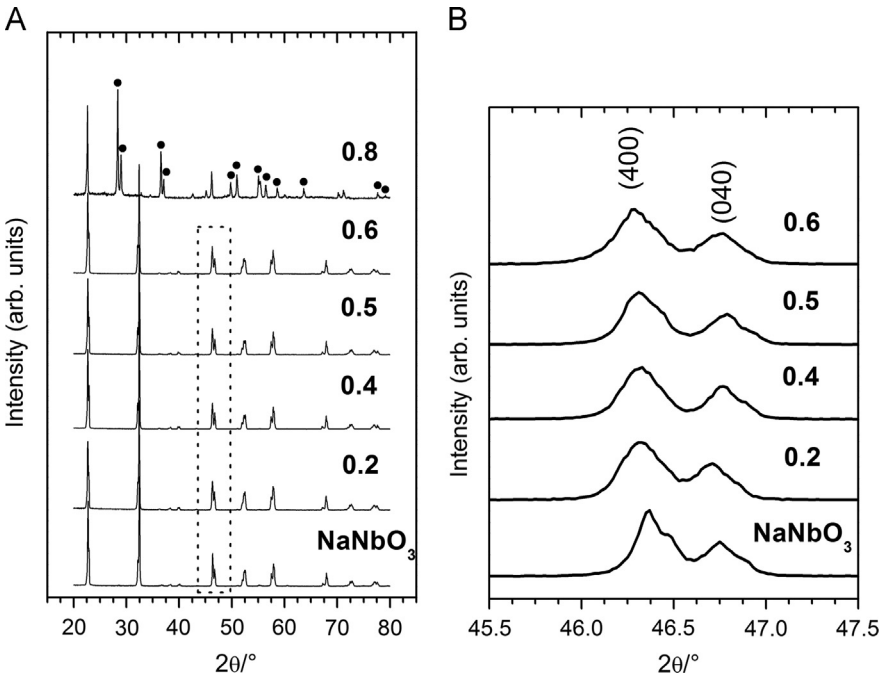

Fig. 1. Influence of the KOH/(KOH+NaOH) ratio in the structure of the KNN obtained by hydrothermal synthesis: (A) XRD patterns of KNN obtained from different (0–0.8) KOH/(KOH+NaOH) ratios in 4 N concentration and (B) magnification of the 45.5–47.5° 2θ range. ●Nb_2O_5.

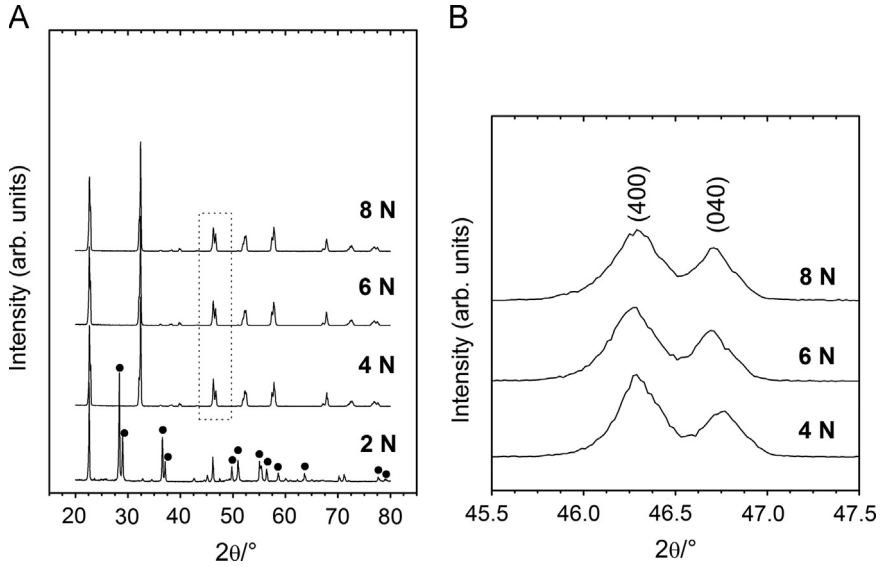

Fig. 2. Effect of the hydroxide concentration on the structure of the obtained KNN: (A) XRD patterns of KNN obtained from different (2–8 N) total hydroxide concentrations. ●Nb_2O_5 and (B) magnification of the 45.5–47.5° 2θ range.

coexist with different distortions. Diffraction patterns of samples synthesized in the presence of KOH are clearly different from that of the $NaNbO_3$ phase, as can be observed in Fig. 1(B). According to these results, the sample obtained with a 0.6 · KOH/(KOH+NaOH) ratio and 4 N hydroxide concentration presented the highest amount of K^+ cations in the crystalline lattice ($K_{0.1}Na_{0.9}NbO_3$). After this observation, new syntheses were carried out at 190 °C with a 0.6 KOH/(KOH+NaOH) ratio and different total hydroxide concentrations in order to completely dissolve the reagents and to increase the amount of K^+ in the crystalline lattice. Fig. 2(A) shows the XRD patterns of $K_xNa_{1-x}NbO_3$ obtained using total (KOH+NaOH) hydroxide concentrations between 2 and 8 N. KNN did not crystallize under a 2 N hydroxide concentration. This result suggests that low hydroxide concentrations do not dissolve Nb_2O_5 at the selected temperature. Diffraction patterns from samples obtained at higher OH^- concentrations are associated with the $K_{0.1}Na_{0.9}NbO_3$ (JCPDS 074-2025) phase. Analyzing the peaks between 45.5° and 47.5° 2θ, it can be concluded that samples belong to similar crystalline structures, see Fig. 2(B). Samples obtained from hydroxide concentrations 6 and 8 N show peaks shifted to lower 2θ angles with respect to the sample obtained with a 4 N

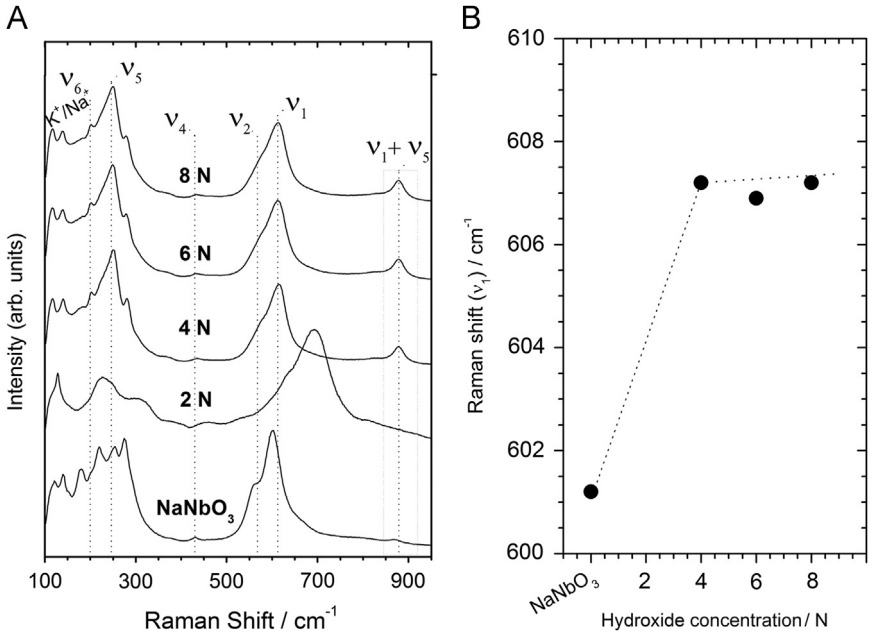

Fig. 3. (A) Raman spectra of the powders obtained with a constant KOH/(KOH+NaOH) ratio of 0.6 and 2 to 8 N total hydroxide concentrations and (B) Position of the ν_1 band as the function of hydroxide concentration.

concentration. This may indicate that higher concentrations of hydroxide favored the incorporation of K^+ cations into the solid solution. Then, the lattice parameters were refined using the monoclinic point group C2/M and revealed a limited evolution of the lattice parameters, $a=3.918$ Å, $b=3.889$ Å, $c=3.923$ Å, and $\beta=89.47°$, for systems with 0.6 KOH/(KOH+NaOH) ratios and 8 N total OH^- concentration, which is close to the system prepared with a 4 N hydroxide concentration.

Samples prepared under different hydroxide concentrations were examined by Raman spectroscopy in order to gain additional structural information. The obtained spectra are shown in Fig. 3(A). Spectra from samples obtained with 4–8 N hydroxide concentrations match well with $K_xNa_{1-x}NbO_3$ in agreement with the related literature [24]. Furthermore, in systems synthesized under higher OH^- (>4 N) concentrations, four main bands due to vibration modes characteristic of KNN, and associated with NbO_6 octahedron, can be observed. These are located at 250, 560, 615 and 860 cm^{-1}, and are identified as ν_5, ν_2, ν_1 and $\nu_1+\nu_5$ Raman modes, respectively. In particular, A_{1g} (ν_1) and F_{2g} (ν_5) Raman modes due to relatively strong scattering in systems similar to KNN, because of a nearly-perfect equilateral octahedral symmetry [25–27]. It is important to mention that the band referred to as $\nu_1+\nu_5$ in Fig. 3(A) does not appear in the Raman spectrum of $NaNbO_3$, therefore confirming the presence of K^+ cations in the lattice and KNN formation [28]. On the other hand, Fig. 3(A) shows that the 2 N sample does not consist in the expected KNN crystalline structure; the recorded spectrum does not match with that reported for $K_xNa_{1-x}NbO_3$. These results have also been confirmed by XRD, as shown in Fig. 2.

Fig. 3(B) shows the variation in the ν_1 mode as the function of OH^- concentration. Clearly, the position of the vibration mode ν_1 shifts to higher wavenumber when the concentration of OH^- increases from 2 N ($NaNbO_3$) due to an increase in the bond strength caused by the shortening of the distance between B^{5+}-type ions and oxygen [29]. Then, the A_{1g} (ν_1) Raman mode shift is in agreement with the evolution of the structural distortion parameter observed by XRD, as shown in Fig. 2. The K^+ cations compete with Na^+ cations in the occupancy of A sites of the ABO_3 perovskite to form a solid solution, especially at higher OH^- concentrations. The large distortion caused by the incorporation of K^+ cations modifies the structure of the solid solution. High OH^- concentrations (>4 N) led to almost the same position for ν_1, suggesting that the bond strength has reached a stable value and that it depends on potassium concentration.

Fig. 4(A–C) corresponds to SEM micrographs of the powders obtained by hydrothermal reaction, which show that the average size of the obtained particles is about 1 μm. The particles have a typical feature of cubic shaped particles, which is common in KNN-based ceramics. Particle size distributions of the samples are shown in the insets of Fig. 4(A–C). For 4 N hydroxide concentration a slightly broad particle size distribution was obtained. As hydroxide concentration increases, the particle size distribution shifts towards unimodal shape and the particle size decreases, as shown the insets in Fig.4(B–C). The increase of hydroxide concentration in the reaction medium promotes the hydrolysis of Nb_2O_5 and causes the particle size distribution to become narrower. From the perspective of the interparticle growth, it can be observed that the system has a different behavior with respect to the evolution observed in the particle size. High hydroxide contents seem to facilitate the nucleation of large crystals by means of the assembly (or secondary nucleation) of small crystals. Finally, the process of the interparticle growth is illustrated by the Scheme in Fig. 4(D). The mechanism can be described as the formation of interfaces between small particles, which are highly stable and modified only with the

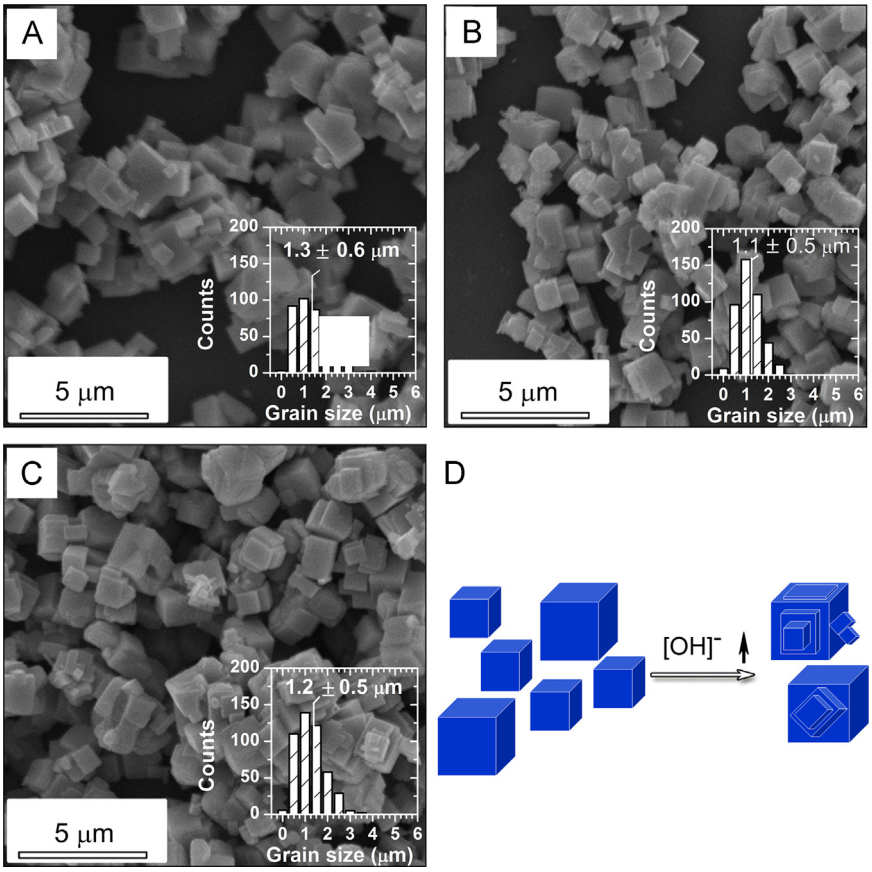

Fig. 4. Microstructural characterization of primary particles of the KNN synthesized by the hydrothermal method: SEM images of samples synthesized with hydroxide concentrations (A) 4 N; (B) 6 N and (C) 8 N. The insets show the particle size distributions of KNN samples. (D) Schematic representation of the formation process of KNN particles with increasing hydroxide concentration.

increase in the hydroxide concentration. The effect of this behavior on the sintered samples will be described in the following section (Fig. 5).

3.2. Characterization of sintered samples

Fig. 5(A–C) shows SEM micrographs of the sintered samples prepared from powders obtained with different hydroxide concentrations, along with the respective grain size distribution diagrams. A change of the average grain size and grain morphology is observed with the hydroxide content, as depicted in Fig. 5(A and C). Samples are composed of grains from 3 to 6 μm with well-defined grain boundaries. In the size distribution diagrams it can be observed that the grain size increases with the hydroxide content. The average grain size increases from $\sim 5.4 \pm 3.8$ μm in the sample from low hydroxide concentration (4 N) to $\sim 7.1 \pm 3.2$ μm for hydroxide contents higher than 6 N. For concentrations higher than 6 N, the average grain size remains almost constant. For the 4 N hydroxide concentration, the KNN ceramic system has a broad bimodal grain size distribution. As a consequence, these distributions are fitted to the sum of two Gaussian functions. As the hydroxide content increases, the grain size distribution shifts towards higher grain sizes. The presence of K^+ cations in the composition causes the grain size distribution to become unimodal. Therefore, this evolution evidences a logical relationship between the interparticle growth mechanism, as illustrated in Fig. 4, and the grain size of the ceramics: the higher the formation of interfaces between small particles of the system, higher grain sizes and narrower size distributions result in sintered samples.

SEM images in Fig. 5 show sintered ceramics with low porosity, in which pores are located mainly at grain boundaries and triple points. Triple points close to 120° indicate the final stage of sintering where pores are removed by diffusion. The incorporation of K^+ cations into the composition induces the evolution of grain morphology to nearly rectangular shaped grains with triple point angles of 90°. The secondary nucleation of small crystals improved the surface diffusion mechanisms that promoted the formation of the characteristic rectangular KNN grains. Considering the usual densification problems of KNN, these samples present a high degree of densification [4,25]. High density values are attained in virtue of the synthesized powder, whose nanosized particles determine its reactivity. Furthermore, the sample density slightly increases with the hydroxide concentration and the K^+ content as shown in Table 1.

High density ceramics are perfectly adapted to measure the dielectric and ferroelectric properties. Concerning the electrical properties of sintered samples, real permittivity (ε') and loss

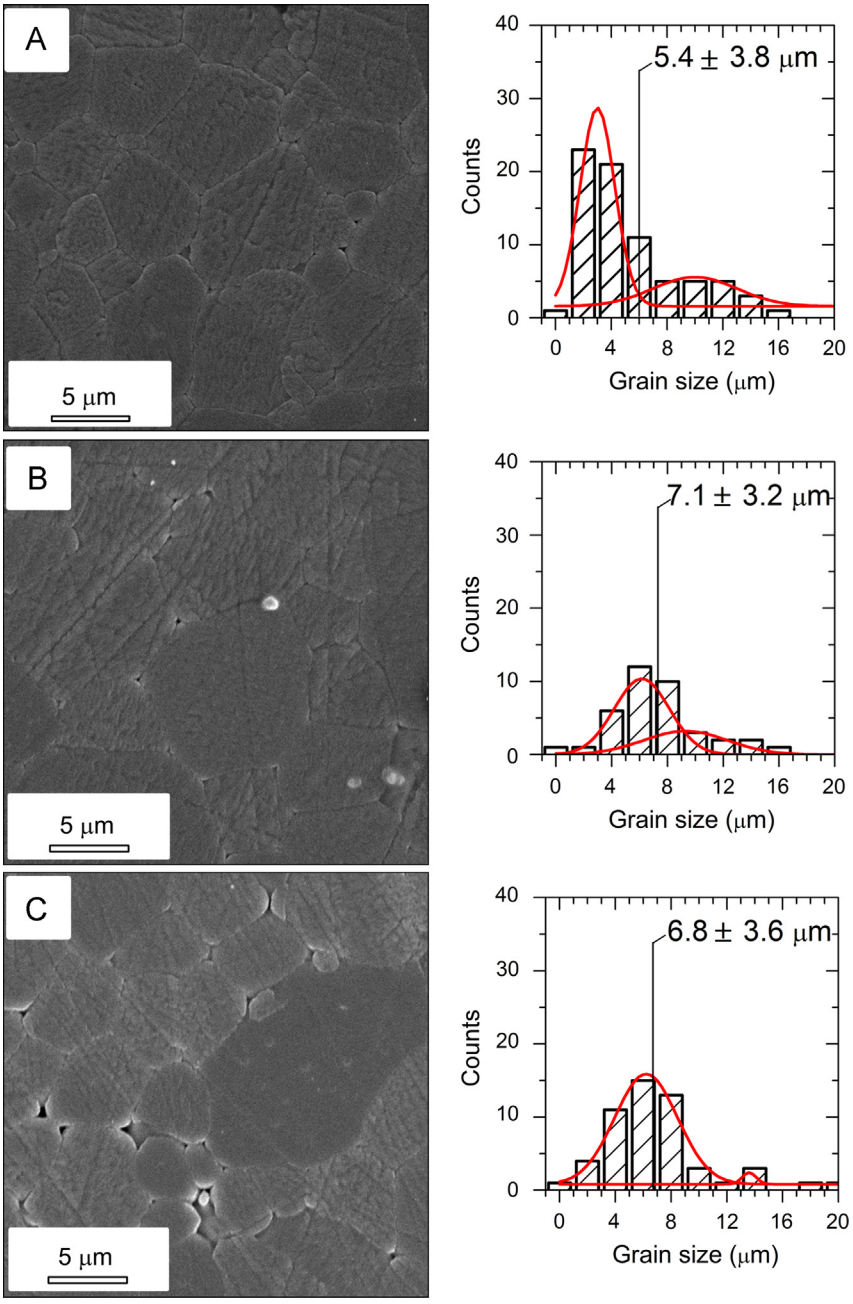

Fig. 5. Microstructure of polished and thermally etched surfaces of KNN sintered samples obtained from powders synthesized with different total hydroxide concentrations (A) 4, (B) 6 and (C) 8 N. The grain size distributions are also shown. The average grain size was determined from FE-SEM micrographs by an image processing and analysis program considering more than 100 grains in each measurement. The distributions were fitted to the sum of two Gaussian functions.

tangent (tan (δ)) curves are shown in Fig. 6(A) and (B), respectively, as the function of frequency and reaction conditions. These results are also summarized in Table 1. In general, real permittivity and losses decrease with frequency. This behavior is more pronounced for the sample obtained from the powder synthesized with a 4 N hydroxide concentration, maybe due to the low sample density. The increase of ε' and tan (δ) at low frequencies for polar materials, can be attributed to the contribution of multi component polarization mechanisms (i.e. electronic, ionic, orientation and space charge) [30]. At high frequencies the dipoles cannot rotate rapidly, so that their oscillations lag behind those of the field [31]. As the frequency is further increased, the dipole will be completely unable to follow the field and the orientation polarization ceases, so ε' decreases and reach a constant value at high frequencies due to the interfacial polarization [32].

Table 1
Apparent density (ρ), real permittivity (ε') and loss tangent (tan (δ)) at 10 kHz of KNN samples obtained under different total hydroxide concentrations.

[KOH + NaOH] (N)	ρ (g/cm^3)	ε'	tan (δ)
4	3.95	158	0.06
6	4.23	165	0.03
8	4.33	176	0.03

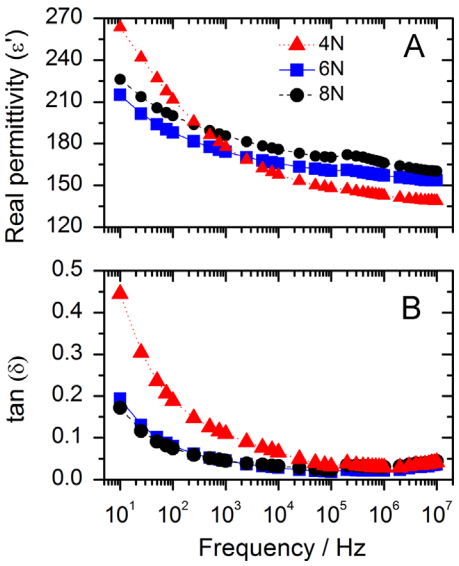

Fig. 6. Variation of the real part of Permittivity (ε') (A) and loss tangent (tan (δ)) (B) with frequency for samples synthesized with total hydroxide concentrations equal to 4, 6 and 8 N and with a constant KOH/(KOH+NaOH) ratio of 0.6.

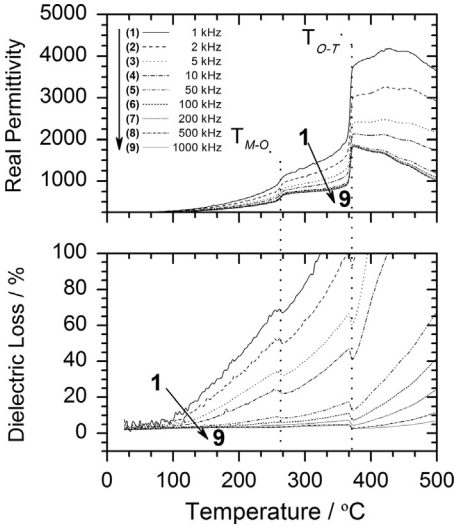

Fig. 7. Real permittivity (top) and dielectric loss (bottom) as a function of frequency and temperature for samples synthesized with total hydroxide concentrations equal to 8 N with a 0.6 KOH/(KOH+NaOH) ratio.

The temperature dependence of the real permittivity and the dielectric loss of samples obtained using a hydroxide concentration of 8 N is shown in Fig. 7(top) and (bottom), respectively. The dielectric properties were measured over a wide temperature range from 25 °C to 500 °C at different frequencies. Peak anomalies of the dielectric constant are shown at about 380 °C and 270 °C. These transition temperatures could be related to the monoclinic–orthorhombic phase transition observed at ~270 °C and orthorhombic–tetragonal phase transition registered at 365 °C, respectively. The herein obtained values are closer to transformation temperatures of $NaNbO_3$ than of $KNbO_3$, suggesting that these ceramics have a high concentration of $NaNbO_3$ or that $x < 0.5$ in $K_xNa_{1-x}NbO_3$ [23].

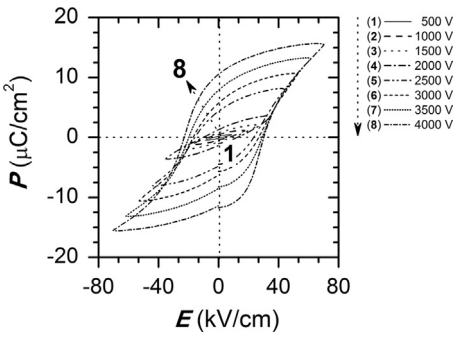

Fig. 8. Hysteresis loops at room temperature for samples obtained with total hydroxide concentration of 8 N with a 0.6 KOH/(KOH+NaOH) ratio.

The specimens with high density sintered from powders obtained with 8 N hydroxide concentration, were also analyzed under an external strong electric field, exhibiting in all cases ferroelectric behavior due to spontaneous polarization. The polarization hysteresis loops of KNN ceramics at room temperature and under an electric field sweep (up to $E_p = 40$ kV/cm) are shown in Fig. 8. The obtained results, well-saturated shape, a coercive electric field (E_c) of 31 kV/cm, a saturation polarization of 16 μC/cm^2, and high remnant polarization (P_r) of 11 μC/cm^2, indicate good ferroelectric properties.

3.3. Characterization of the domain structure by Confocal Raman Spectroscopy (CRM)

Groups of unit cells with the same orientation are called ferroelectric domains. Because of the random distribution of the domain orientations in ceramic materials, no macroscopic piezoelectric behavior is observable. Due to the ferroelectric nature of the KNN material, it is possible to force permanent reorientation and alignment of the different domains using a strong electric field, as shown in Fig. 8. At the improving of properties one of the major concerns is the increase of piezoelectric coefficient d_{33}, which is determined by the electric charge response to a low external mechanical stress under linear conditions. The low mechanical field applied in the d_{33} measurement inhibited the extrinsic contribution of non-180° domain wall motions, so the d_{33} values are dominated by the intrinsic (lattice) piezoelectric responses. Thus, the study of domain walls in piezoelectric materials is critical for a better understanding of their properties. To identify the structure of ferroelectric domains in KNN ceramics, we propose using Confocal Raman Spectroscopy (CRM) because methods based on micro-Raman spectroscopy give the possibility of studying the structural deformations of perovskite at a local scale, which are induced both by the tilting of BO_6 octahedra and by the cationic displacements.

Fig. 9(A) shows an optical micrograph of the polished and thermal etched (950 °C for 5 min) surface of the ceramic placed perpendicularly to the laser beam. Specimens with high density (from powders 8 N) are analyzed. Raman spectra are collected from a 16×20 μm^2 selected area on a plane located just below the surface of the sample where the Raman intensity is maximized. The acquisition time for a single Raman

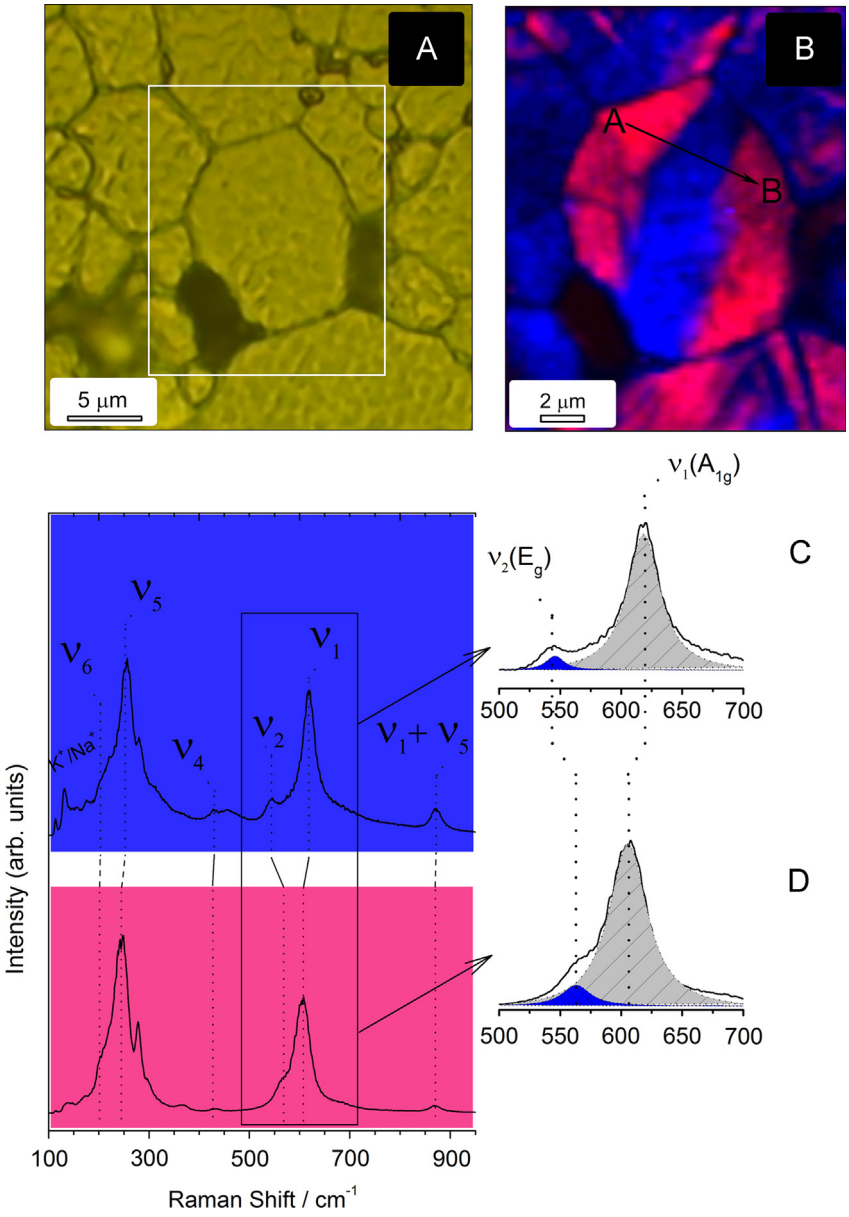

Fig. 9. Confocal Raman Spectroscopy characterization of KNN ceramics with 8 N total hydroxide concentration and 0.6 KOH/(KOH+NaOH) ratio: (A) Optical micrograph of the polished surface of KNN. (B) Raman image of KNN exhibiting the domain structure. This image resulted from the different single Raman spectra collected from each pixel. Raman spectra having same spectral shift for the Raman modes were color identified. The intensity of the color is correlated with the Raman intensity. (C and D) Main Raman spectra associated with different colors. The insets show magnified Raman spectra fitted by the sum of two Lorentzian peaks, ascribed to the E_g (υ_2) and A_{1g} (υ_1) Raman modes, respectively. (For interpretation of the references to color in this figure, the reader is referred to the web version of this article.)

spectrum is 500 ms, thus the acquisition of a Raman image consisting of 64×80 pixels (5120 spectra) requires 43 min. Features such as Raman peak intensity, peak width or Raman shift from the recorded Raman spectra are fitted with algorithms to compare information and to represent CRM images, Fig. 9(B). According to the nuclear site group analysis, Raman active vibrations of the of the BO_6 octahedron are represented by $1A_{1g}$ (υ_1)+$1E_g$ (υ_2) +$2F_{1u}$ (υ_3, υ_4)+F_{2g} (υ_5)+F_{2u} (υ_6) modes [30]. Among these vibrations, $1A_{1g}$ (υ_1)+$1E_g$ (υ_2) +$1F_{1u}$ (υ_3) are stretching modes and the rest, bending modes [31]. In particular, A_{1g} (υ_1) symmetrical mode and F_{2g} (υ_5) antisymmetric mode are detected as relatively strong scattering signals in KNN based materials because of a near-perfect equilateral octahedral symmetry. Raman spectra having same Raman shift are classified by colors correlating the color intensity with the Raman intensity. The combination of colors results in an image of the ceramic microstructure which reveals the presence of a ceramic grain with striped ferroelectric domains. This Raman image provides a scenario to study the domain structure in polycrystalline samples synthesized by the hydrothermal method.

In a pioneering study concerning the structure of ferroelectric domains in (K,Na)NbO_3 single crystals [32], the appearance of an unusual polarization relaxation at the 90°

domain wall due to the coexistence of tetragonal and orthorhombic domains is demonstrated 90° and 180° pre-existing tetragonal domains constrain the appearance of room temperature orthorhombic domains and alternating polarization differences in domain tetragonal templates are resolved by 60° and 120° orthorhombic domains.

The colors in the Raman image are coded accordingly with their corresponding spectra in which two different main Raman spectra (blue and magenta) could be identified, Fig. 9. The revealed Raman modes are certainly coupled on the ceramic material and the accuracy in the determination of crystal orientation in adjacent regions is not completely attainable with the above measurements only. Interestingly, the domain loses the striped shape in the interior of the large grain where the grain boundary constrains the domain wall. Absence of S-type domains typical of the orthorhombic domains it is not observed in the Raman image. As previously stated [34] the high temperature orthorhombic phase acts as a template to the appearance of 60° and 120° monoclinic domains. But in this case the stresses modified the former orthorhombic stripped domains and the stress accommodation due to the appearance of non-180° domains account for the new observed ferroelectric domain.

Fig. 9(C) and (D) shows the average Raman spectra obtained from two adjacent domains, as shown in Fig. 9(B). Clear differences can be observed in the shape of both spectra, particularly in the 500 to 700 cm^{-1} region. The details of the NbO_6 octahedron E_g (υ_2) and A_{1g} (υ_1) stretching Raman modes of the perovskite are magnified in the insets in Fig. 9(C–D) and fitted by the sum of two Lorentzian peaks. The A_{1g} (υ_1) mode located at $\sim$614 cm^{-1} is a symmetric mode, the Lorentzian peaks with grey fill color. So, it is observable for the different crystal orientations and it is usually an intense mode, whereas the E_g (υ_2) Raman mode at $\sim$550 cm^{-1} is an anti-symmetric Raman mode, the Lorentzian peaks with blue fill color, along the polar direction (perpendicular to the basal plane). The E_g (υ_2) Raman mode is less intense than the A_{1g} (υ_1) in both spectra, see blue spectrum (Fig. 9C) and magenta spectrum (Fig. 9D). The E_g (υ_2) mode is magnified when the laser polarization is parallel to the polar direction. Then, the polar direction is nearly perpendicular to the sample (out of plane polarization) in regions where the blue spectrum is present, Fig. 9(C). Surprisingly, the magenta region is also having a nearly out of plane polarization. In principle the adjacent domains should be separated by a 90° domain wall. The differences between both regions could be stated after an analysis of the Raman shift values of E_g (υ_2) and A_{1g} (υ_1) modes. The blue spectrum region possesses a higher Raman shift for the A_{1g} (υ_1) Raman mode that accounts for an increase in binding energy strength caused by the shortening of the distances between Nb^{5+} and its coordinated oxygen [30]. On the other hand, the lower Raman shift for E_g (υ_2) indicates a softening of the polarization. This softening is associated with the higher intensity of the alkaline translational Raman modes versus NbO_6 octahedra observed at $\sim$155 cm^{-1}. The observed differences correlated with the existence of two different symmetries in adjacent domains. The Na^+ rich regions possess monoclinic distortion in which the polar direction makes an angle of a few degrees from the [101] direction. The higher distortion of the monoclinic phase produces a higher Raman shift of the A_{1g} (υ_1), the softening in the E_g (υ_2) Raman mode and the increased polarizability of translational modes, so the blue regions could be associated with more distorted regions. The incorporation of K^+ cations into the composition stabilized the orthorhombic structure in which the polarization in the crystal lattice is in the [101] or [011] directions, which causes both the red shift of the A_{1g} (υ_1) and the blue shift of the Eg (υ_2) Raman modes. To sum up, CRM allows the determination of monoclinic regions (blue regions in the Raman image) and orthorhombic regions (magenta regions in the Raman image). Orthorhombic domains locate at the grain boundaries, and account for K^+ diffusion during the grain growth at the sintering stage. The presence of secondary crystallization of small particles during the hydrothermal synthesis in large KOH/(KOH+NaOH) ratio and hydroxide concentration could be thus related to the enhancement of diffusion by the presence of reactive particles. Moreover, the K^+ diffusion could favor the domain wall constrain by the grain boundaries.

The first domain structure appears during the cooling from the high temperature cubic symmetry to tetragonal phase. At this step, the adjacent domains should be separated from a 90° domain wall. The further cooling of the sample induces the appearance of orthorhombic (or monoclinic) domains in the tetragonal domains that act as templates. For this reason we would refer to the domain wall between blue and magenta regions, as 90° domain wall. Beside the conclusions derived from the comparison of the Raman intensity between different Raman modes, an exhaustive examination of the Raman spectra has also allowed us to find other remarkable features related to the Raman mode-shifting on the different KNN adjacent domains separated by a 90° domain wall. To evidence the difference between the adjacent domains separated by a 90° domain wall the following experiment was conducted and the results are shown in Fig. 10. At the beginning, Raman spectra were measured following a line crossing perpendicularly to the domain wall direction (see the line as A→B in Fig. 9(B)) where out-of-plane directions are coexisting corresponding to different in symmetry spectra 9(C) and 9(D) respectively.

From Fig. 10(A), three strategic points were selected along the line direction (denoted as 1, 2, and 3). These three regions correspond to two adjacent domains (1 and 3) and their 90° domain wall (2) that intersects both domains. Fig. 10(B) shows the detail of the NbO_6 octahedron Raman modes, marked as 1, 2 and 3 in Fig. 10(A and B). It is worth to notice a characteristic aspect in the A_{1g} and E_g Raman shift evolution along the line crossing the domains. The Raman shift changes are opposite in sign between both modes (a polarization change, probably attributed to differences in polarization orientation, is compensating between both modes). This clear evidence indicates that, in addition to the polar orientation change (evaluated by Raman Intensity), the value of cell distortion is also modified and therefore the polarization and/or stress changes (in value as well as in orientation). These

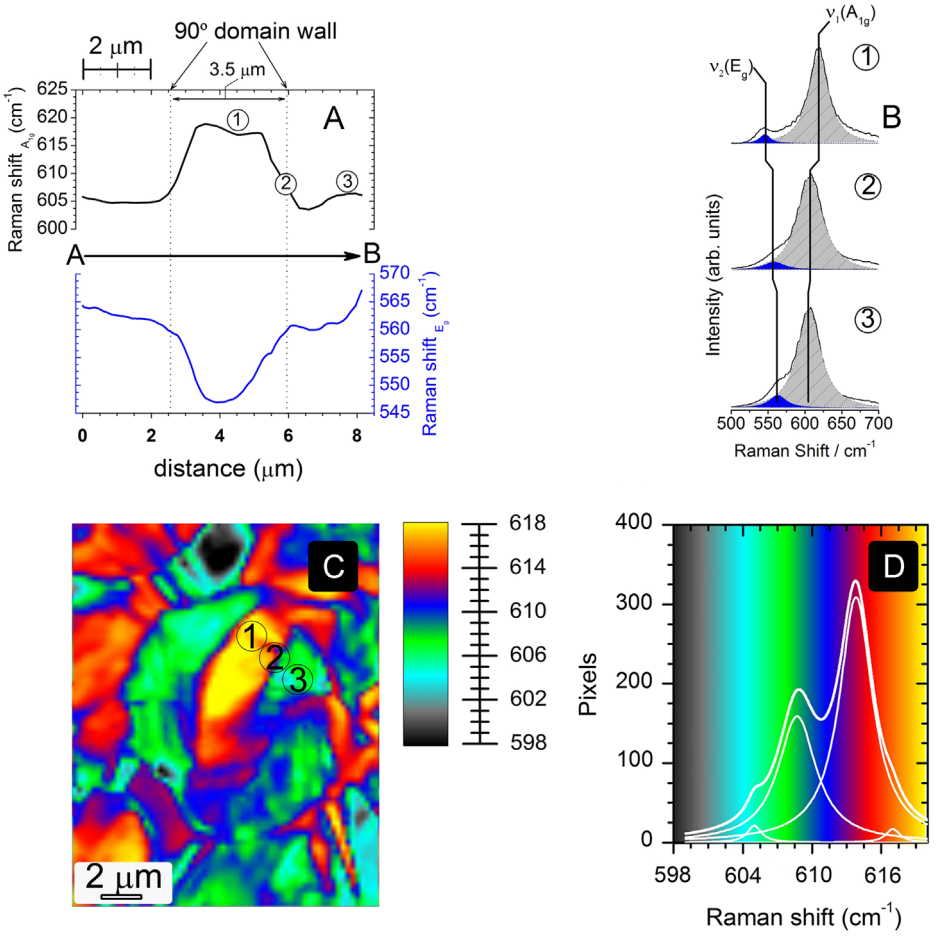

Fig. 10. Evaluation of distortion and stress on the domain structure of KNN by Confocal Raman Spectroscopy: (A) Evolution of the Raman shift of E_g and A_{1g} modes, which were measured following the black arrow in Fig. 9(B). (B) Magnified Raman spectra and Lorentzian fits of domain structure in the 500–700 cm^{-1} frequency range corresponding to the points labeled 1, 2 and 3 in the image in (A). These spectra are fitted to the sum of two Lorentzian peaks, ascribed to the E_g (ν_2) and A_{1g} (ν_1) modes, respectively. (C) Color-coded map showing the Raman shift corresponding to the A_{1g} mode. The points labeled 1, 2 and 3 correspond to the different regions shown in (A). The color code bar corresponds to values of Raman shift determined at each pixel. (D) Statistical analysis of the spectra corresponding to different Raman shift values of the A_{1g} mode. (For interpretation of the references to color in this figure, the reader is referred to the web version of this article.)

observed changes allow evaluating the distribution, width and the nature of the domains along the marked line by studying the Raman shift variation along it, see Fig. 10(A). The analyses also confirm that the domains width ranged from 3 to 3.5 μm. Moreover, an abrupt decrease in the Raman shift of the A_{1g} mode (or an increase in the Raman shift of the E_g mode) occurs in the 90° domain wall with a softening $> 12\ cm^{-1}$ compared with that observed in the interior of monoclinic domains. A similar effect on the 90° domain wall has been observed in single crystals, which is associated with the decrease of polarization at 90° domain walls as a consequence of the accumulated stress [33]. Thus, the effect in ceramics may be of the same origin but the grain boundaries constrain affect the symmetry of the domain. This behavior is due to the micrometric grain size in KNN ceramics which limits the stress release and results in higher domain wall density. And as a consequence, the stress in samples with fine grains is higher than the one originated in single crystals.

From the perspective of the polarizability of the bonds and keeping in mind the direct correlation between NbO_6 distortion and the remnant polarization (P_r) in modified KNN ceramics [34], the experimental results can be interpreted as follows. The correlation between the Raman shift and P_r was also stated in KNN single crystals by Inagaki et al. [35] who considered that the appearance of 60° domains at slow-cooling thermal treatment is favorable for stress releasing and as a consequence the polarization enhancement.

In order to identify the polarization distribution or the stress distribution in the KNN ceramic, a map showing the A_{1g} mode Raman shift was designed and it is shown in Fig. 10(C). Raman imaging allows evaluating the polarization because each pixel comprises a full Raman spectrum. The analyses of the Raman shift of the A_{1g} mode also denote additional features related the variation of Raman shift among the different observed symmetries. These differences are associated with non-90° domains in each adjacent domain or in adjacent grains. However, the analysis of the A_{1g} Raman shift allows a direct comparison of the ferroelectric domains. The statistical analysis of the number of pixels versus A_{1g} mode Raman shift is shown in Fig. 10(D). From Fig. 10(D), the first

and second maximum Raman shift (region between 618 and 613 cm^{-1}, marked in yellow and red) occur at ~31% of the total measured area, and is located in the interior of the large grain, a region referred to as 1 in Fig. 10(C) which corresponds to monoclinic regions. The third and fourth maximum Raman shift (in the 602–613 cm^{-1} range marked in blue and green) account for ~69% of the total area, which correspond to the orthorhombic regions. In each type of domains there is also a stress gradient that produces different Raman shifts according to the stress distribution in the ferroelectric ceramics.

In summary, two interesting observations can be pointed out: firstly, the domain wall formation is aimed to reduce the stress accumulation produced by the coexistence of different symmetries; and secondly, the micrometric grain size in KNN ceramics limits the stress release and results in higher domain wall density in which grain boundaries constrain the domain walls. The understanding of the domain structure plays a crucial role in KNN-modified ceramics, and thus an effective tool to optimize piezoelectric properties in lead free ceramics.

4. Conclusions

Microstructural and electrical properties of $K_xNa_{1-x}NbO_3$ obtained by hydrothermal synthesis have been studied as a function of KOH/(KOH+NaOH) ratio and hydroxide concentration (2–8 N). The following conclusions are derived from this study.

The XRD patterns revealed Na-rich compositions in agreement with the $K_{0.02}Na_{0.98}NbO_3$ and $K_{0.1}Na_{0.9}NbO_3$phases. The *K* concentration in the lattice increases with increasing KOH concentration.

XRD and Raman spectroscopy show that samples obtained with 0.8 KOH/(KOH+NaOH) ratio and 4 N total hydroxide concentration do not have a $K_xNa_{1-x}NbO_3$ typical structure, suggesting the difficulty of potassium to become part of the lattice. Materials obtained from low hydroxide concentrations (2 N) do not have a rich K^+ phase. This is associated with the existence of a critical hydroxide concentration and reaction temperature in order to dissolve Nb_2O_5. Sintered samples obtained from powders synthesized under 8 N total hydroxide concentration showed the highest density values and better dielectric behavior.

Confocal Raman Spectroscopy analyses allowed determining that the domain wall formation aims to reduce the stress accumulation produced by the coexistence of monoclinic and orthorhombic symmetries. In addition, the micrometric grain size in KNN ceramics limits the stress release and results in higher domain wall density. The improvement of piezoelectric properties in the modified KNN is founded on a domain structure that could be designed by using adequate strategies for domain engineering.

Acknowledgments

This work is financially supported by CONICET, ANCPyT (Argentina) and MICINN project MAT 2010–21088-C03-01. Dr. F. Rubio-Marcos is also indebted to CSIC for a "Junta de Ampliación de Estudios" contract (Ref. JAEDOC071), which is co-financed with FEDER funds.

References

[1] T. Morita, Piezoelectric materials synthesized by the hydrothermal method and their applications, Materials 3 (2010) 5236–5245.
[2] R. López-Juárez, O. Novelo-Peralta, F. González-García, F. Rubio-Marcos, M. Villa Fuerte-Castrejón, Ferroelectric domain structure of lead-free potassium-sodium niobate ceramics, J. Eur. Ceram. Soc. 31 (2011) 1861–1864.
[3] J.-H. Lv, M. Zhang, M. Guo, W.-C. Li, X.-D. Wang, Hydrothermal synthesis and characterization $K_xNa_{1-x}NbO_3$ powders, Int. J. Appl. Ceram. Technol. 4 (2007) 571–577.
[4] J. Tellier, B. Malic, B. Dkhil, D. Jenko, J. Cilensek, M. Kosec, Crystal structure and phase transitions of sodium potassium niobate perovskites, Solid State Sci. 11 (2009) 320–324.
[5] A. Chowdhury, J. Bould, J. Londesborough, M.G.S. Milne, Fundamental issues in the synthesis of ferroelectric $Na_{0.5}K_{0.5}NbO_3$ thin films by sol–gel processing, Chem. Mater. 22 (2010) 3862–3874.
[6] J.B. Lim, S. Zhang, J.-H. Jeon, T.R. Shrout, (K,Na)NbO_3-based ceramics for piezoelectric hard lead-free material, J. Am. Ceram. Soc. 93 (2010) 1218–1220.
[7] J. Taub, L. Ramajo, M.S. Castro, Phase structure and piezoelectric properties of Ca- and Ba-doped $K_{1/2}Na_{1/2}NbO_3$ lead-free ceramics, Ceram. Int. 39 (2012) 3555–3561.
[8] R. López-Juárez, R. Castañeda-Guzmán, F. Rubio-Marcos, M.E. Villafuerte-Castrejón, E. Barrera-Calvad, F. González, Insights into the dielectric and luminescent properties of $Na_{0.5}Pr_{0.003}Bi_{0.497-x}La_xTiO_3$ synthesized by the Pechini method, Dalton Trans. 42 (2013) 6879–6885.
[9] J.T. Zeng, K.W. Kwok, H.L. Chan, $K_xNa_{1-x}NbO_3$ powder synthesized by molten-salt process, Mater. Lett. 61 (2007) 409–411.
[10] B. Zhang, J. Wu, X. Cheng, X. Wang, D. Xiao, J. Zhu, X. Wang, X. Lou, Lead-free piezoelectrics based on potassium–sodium niobate with giant d_{33}, Appl. Mater. Interfaces 5 (2013) 7718–7725.
[11] S. Wiegand, S. Flege, O. Baake, W. Ensinger, Influence of different heat treatment programs on properties of sol–gel synthesized $(Na_{0.5}K_{0.5})NbO_3$ (KNN) thin films, Bull. Mater. Sci. 35 (2012) 745–750.
[12] C.-H. Ahn, C.-S. Park, R. Dittmer, S.-H. Hong, S. Priya, Effect of elemental diffusion on temperature coefficient of piezoelectric properties in KNN-based lead-free composite, J. Mater. Sci. 45 (2010) 3961–3965.
[13] G. Demazeau, Solvothermal processes: definition, key factors governing the involved chemical reactions and new trends, Z. Naturforsch. 65b (2010) 999–1006.
[14] D.-Y. Jeong, S.-H. Lee, H.-C. Song, K.-H. Choi, J.-H. Cho, Hydrothermal synthesis and microwave sintering of $(K_{0.5}Na_{0.5})NbO_3$ ceramics, J. Korean Phys. Soc. 58 (2011) 663–667.
[15] F. Zhang, L. Han, S. Bai, T. Sun, T. Karaki, M. Adachi, Hydrothermal synthesis of (K,Na)NbO_3 particles, Jpn. J. Appl. Phys. 47 (2008) 7685–7688.
[16] L. Li, Y.-Q. Gong, L.-J. Gong, H. Dong, X.-F. Yi, X.-J. Zheng, Low-temperature hydro/solvothermal synthesis of Ta-modified $K_{0.5}Na_{0.5}NbO_3$ powders and piezoelectric properties of corresponding ceramics, Mater. Design 33 (2012) 362–366.
[17] T. Lusiola, F. Bortolani, Q. Zhang, R. Dorey, Molten hydroxide synthesis as an alternative to molten salt synthesis for producing $K_{0.5}Na_{0.5}NbO_3$ lead free ceramics, J. Mater. Sci. 47 (2012) 1938–1942.
[18] J. Ortiz-Landeros, C. Gómez-Yáñez, R. López-Juárez, I. Dávalos-Velasco, H. Pfeiffer, Structural and thermochemical chemisorption of CO_2 on $Li_{4+x}(Si_{1-x}Al_x)O_4$ and $Li_{4-x}(Si_{1-x}V_x)O_4$ solid solutions, J. Phys. Chem. A 116 (2012) 3163–3171.
[19] J.A. Lima, T.C. Freire, R.J.C. Lima, A.J.D. Moreno, J. Mendes Filho, F.E.A. Melo, Raman scattering of L-valine crystals, J. Raman Spectrosc. 36 (2005) 1076–1081.
[20] H.J. Trodahl, N. Klein, D. Damjanovic, N. Setter, B. Ludbrook, D. Rytz, M. Kuball, Raman spectroscopy of (K,Na)NbO_3 and $(K,Na)_{1-x}Li_xNbO_3$, Appl. Phys. Lett. 93 (2008) 262901.

[21] C. Pithan, Y. Shiratori, J. Dornseiffer, F.-H. Haegel, A. Magrez, R. Waser Pithan, Microemulsion mediated synthesis of nanocrystalline $(K_x,Na_{1-x})NbO_3$ powders, J. Cryst. Growth 280 (2005) 191–200.

[22] Y. Shiratori, A. Magrez, C. Pithan, Temperature-induced phase transitions in micro-, submicro-, and nanocrystalline $NaNbO_3$, J. Phys. Chem. C 111 (2007) 18493–18502.

[23] N. Zhang, A.M. Glazer, D. Baker, P.A. Thomas, Structures of $K_{0.05}Na_{0.95}NbO_3$ (50–300 K) and $K_{0.30}Na_{0.70}NbO_3$ (100–200 K), Acta Cryst. B65 (2009) 291–299.

[24] Z. Yu, C. Ang, R. Guo, S. Bhalla, Piezoelectric and strain properties of $Ba(Ti_{1-x},Zr_x)O_3$ ceramics, J. Appl. Phys. 92 (2002) 1489–1493.

[25] F. Rubio-Marcos, M.A. Bañares, J.J. Romero, J.F. Fernández, Correlation between the piezoelectric properties and the structure of lead-free KNN-modified ceramics, studied by Raman Spectroscopy, J. Raman Spectrosc. 42 (2011) 639–643.

[26] F. Rubio-Marcos, J.J. Romero, M.S. Martín-Gonzalez, J.F. Fernández, Effect of stoichiometry and milling processes in the synthesis and the piezoelectric properties of modified KNN nanoparticles by solid state reaction, J. Eur. Ceram. Soc. 30 (2010) 2763–2771.

[27] Y. Gou, K. Kakimoto, H. Ohsato, Phase transitional behavior and piezoelectric properties of $(Na_{0.5}K_{0.5})NbO_3$–$LiNbO_3$ ceramics, Appl. Phys. Lett. 85 (2004) 4121–4123.

[28] H. Pan, G.-S. Zhu, X.-L. Chao, L.-L. Wei, Z. Yang, Properties of $NaNbO_3$ powders and ceramics prepared by hydrothermal reaction, Mater. Chem. Phys. 126 (2011) 183–187.

[29] F. Rubio-Marcos, P. Marchet, T. Merle-Méjean, J.F. Fernandez, Role of sintering time, crystalline phases and symmetry in the piezoelectric properties of lead-free KNN-modified ceramics, Mater. Chem. Phys. 123 (2010) 91–97.

[30] L. Ramajo, R. Parra, M.A. Ramírez, M.S. Castro, Electrical and microstructural properties of $CaTiO_3$-doped $K_{1/2}Na_{1/2}NbO_3$-lead free ceramics, Bull. Mater. Sci. 34 (2011) 1213–1217.

[31] N.A. Hegab, A.E. Bekheet, M.A. Afifi, L.A. Wahaba, H.A. Shehata, Effect of Cd addition on the ac conductivity and dielectric properties of $Ge_{70}Te_{30}$ films, J. Ovonic Res. 3 (2007) 71–82.

[32] D.H. Cho, M.K. Ryu, S.S. Park, S.Y. Cho, J.G. Choi, M.S. Jang, A study of ferroelectric properties in $Na_xK_{1-x}NbO_3$ ceramic compounds, J. Korean Phys. Soc. 46 (2005) 151–154.

[33] K. Kakimoto, K. Akao, Y. Guo, H. Ohsato, Raman scattering study of piezoelectric $(Na_{0.5}K_{0.5})NbO_3$–$LiNbO_3$ ceramics, Jpn. J. Appl. Phys. 44 (2005) 7064–7067.

[34] F. Rubio-Marcos, A. del Campo, R. López-Juárez, J.J. Romero, J.F. Fernández, High spatial resolution structure of $(K,Na)NbO_3$ lead-free ferroelectric domains, J. Mater. Chem. 22 (2013) 9714–9720.

[35] Y. Inagaki, K.-I. Kakimoto, I. Kagomiya, Ferroelectric domain characterization of orthorhombic sodium-potassium niobate piezoelectric crystals, J. Am. Ceram. Soc. 93 (2010) 4061–4065.